Journal of Materials Chemistry A

ROYAL SOCIETY OF CHEMISTRY

PAPER

View Article Online
View Journal | View Issue

Check for updates

Cite this: J. Mater. Chem. A, 2025, 13, 5374

Enhanced degradation of organic contaminants using a PVDF/AC-NaCl piezocatalyst: effect of geometric design in fluid flow environments†

Gunn Park, Se-Chang Oh, Seung-Hyun Kang and Jae-Woo Park *

Received 26th November 2024
Accepted 15th January 2025

DOI: 10.1039/d4ta08365b

rsc.li/materials-a

Technologies to treat water using the piezoelectric effect of polyvinylidene difluoride (PVDF) have attracted significant research attention, with many studies focusing on exploiting the pressure from fluid flow on piezoelectric catalysts. This pressure varies according to catalyst geometry, potentially enhancing the effectiveness of water treatment. Here, we describe the synthesis of a triangular prism of PVDF/activated carbon-NaCl with a piezoelectric strain coefficient of 35 pC N^{-1}, generating a maximum voltage of 5.25 $\times 10^{-1}$ V. This led to the formation of H^+ and ·OH radicals, achieving degradation efficiencies of 99.91%, 97.12%, 95.03%, and 99.53% for rhodamine B, 4-nitrophenol, phenol, and tetracycline, respectively. Energy consumption was 38.67 kW h per m^3 per order, a more efficient value than that produced by a piezocatalyst with a greater piezoelectric strain coefficient and conventional advanced oxidation processes. These findings deepen our understanding of how the efficiency of water treatment in piezocatalysts using fluid flow can vary depending on catalyst geometry and may be used to design other piezocatalysts in fluid flow.

1. Introduction

Piezocatalytic water treatment offers the advantages of low energy consumption and small carbon footprint.[1–4] It can be carried out in the presence of external physical forces without the need for additional oxidants or power sources.[5–8] The physical forces required to drive piezocatalysis can take the form of mechanical vibration, ultrasonication, and fluid flow, among others.[8–14] These driving forces induce polarization, depositing charges on the surface of piezoelectric materials[15] and creating an internal electric field.[16] Electrons and holes move toward the surface of the catalytic structure along this internal electric field.[17] Electrons and holes at the surface then react with water and oxygen molecules, respectively, to generate reactive oxygen species such as hydroxyl radicals (OH·) and superoxide radicals ($\cdot O_2^-$) that contribute directly to the degradation of organic molecules.[18–20]

Base materials of piezocatalysts can be classified into ceramics and polymers.[5,21,22] Polymers are flexible, inexpensive, and nontoxic. They have low operating temperatures with higher piezoelectric voltage coefficients compared with ceramics.[23–25] These characteristics contribute to efficient, versatile, and environmentally friendly piezocatalytic process design. Polyvinylidene fluoride (PVDF) is one of the most commonly used piezoelectric polymers.[26,27]

Fluid flow, a driving force activating the piezoelectric effect in piezocatalysis, can lead to the degradation of organic contaminants.[6,7,14,28–32] A thin coating of Cu_2O@MoS_2/PVDF inside a pipe was found to degrade 99.3% of the norfloxacin in water flowing at 1.289 L min^{-1}.[13] A thin coating of ZnO/carbon quantum dot (CQD)/PVDF inside a pipe was used to degrade 95.36% of the tetracycline (TC) at a water flow of 0.147 m s^{-1}. The energy consumption was only 17.57% of that of ultrasonic systems.[14] Degradation of methyl orange (MO) dye using ZnO-nanorod/PVDF-hexafluoropropylene in a sponge has been reported.[33] A piezoelectric field driven by water stirred at 1000 rpm facilitated the separation and migration of carriers, enhancing the degradation of MO due to ultraviolet (UV) light irradiation for 75 min. A ZnO-nanowire/carbon-fiber catalyst showed evidence of the piezoelectric effect due to the movement of carbon fibers in water, causing the attached ZnO nanowires to collide or bend due to fluid flow. This led to the degradation of 64% of methylene blue dye over 120 min.[34]

Meanwhile, harvesting energy using piezoelectric materials and fluid flow as a driving force has been applied to various designs. Moving, rather than stationary, piezoelectric materials are frequently used. A hydraulic-pressure-driven piezoelectric stack generated up to 1.2 mW from a dynamic ripple pressure of 400 kPa.[35] A wind turbine with a diameter of 42 mm was used to produce 2.4 mW at an air velocity of 5.5 m s^{-1}. This produced 2.6 V at an air velocity of 11.83 m s^{-1}, which is sufficient to split water.[36,37] A broadband rotary piezo-electromagnetic generator can harvest 287 mW m^{-3} of energy while being rotated with fluid flow.[38]

Department of Civil and Environmental Engineering, Hanyang University, Seoul 04763, South Korea. E-mail: jaewoopark@hanyang.ac.kr

† Electronic supplementary information (ESI) available. See DOI: https://doi.org/10.1039/d4ta08365b

However, few studies have reported applications that use moving piezocatalysts for environmental decontamination. We tested the aqueous degradation of rhodamine B (RhB), 4-nitrophenol (4-NIP), phenol, and TC with a PVDF/activated carbon (AC)-NaCl piezocatalyst attached to moving blades. The moving piezocatalyst actively generated fluid flow, unlike the fixed piezocatalysts commonly used in environmental decontamination. The objectives of this research are (1) optimizing the design of the moving piezocatalyst for maximal piezoelectric response using computational fluid dynamics (CFD) analysis, (2) validating the optimized design by investigating the efficiency of the PVDF/AC-NaCl piezocatalyst in degrading various organic contaminants, and (3) assessing the energy efficiency and operational feasibility of the moving piezocatalyst.

2. Experimental methods

2.1 Materials

For this research, PVDF ($(C_2H_2F_2)_n$, $M_w \approx 55\,000$, Sigma-Aldrich, USA), coal-based granular AC (Calgon, $\Phi < 75$ μm, USA), *N*,*N*-dimethylformamide (C_3H_7NO, DMF, Dae-Jung, Korea), acetone (C_3H_6O, J.T. Baker, USA), MO ($C_{14}H_{14}N_3NaO_3S$, Sigma-Aldrich), TC ($C_{22}H_{24}N_2O_8$, Sigma-Aldrich), RhB ($C_{28}H_{31}ClN_2O_3$, Sigma-Aldrich), 4-NIP ($C_6H_5NO_3$, Sigma-Aldrich), phenol (C_6H_6O, Sigma-Aldrich), NaCl (Samchun, Korea), thiourea (CH_4N_2S, Sigma-Aldrich), ethylenediaminetetraacetic acid disodium salt dihydrate ($C_{10}H_{14}O_8N_2Na_2 \cdot 2H_2O$, Daejung, Korea), benzoquinone ($C_6H_4O_2$, BQ, Sigma-Aldrich), 5,5-dimethyl-1-pyrroline-*N*-oxide (DMPO, Sigma-Aldrich), and 2,2,6,6-tetramethyl-1-piperidinyloxy (TEMPO, Sigma-Aldrich) were purchased. All reagents were used without further purification. Deionized water (DI, AquaMAXTM-Ultra370, Young In Chromass, Korea) was also used.

2.2 PVDF/AC-NaCl foam synthesis

The PVDF/AC-NaCl was synthesized using phase inversion, which does not require high-voltage equipment, such as electrical poling, and facilitates the fabrication of complex shapes, flexibility, and porous structures.[39,40] Initially, 12 g of PVDF was dissolved in 60 mL of DMF and 36 mL of acetone in a 300 mL beaker 80 mm in diameter. The mixture was stirred at 200 rpm for 1 h at 25 °C until it changed from opaque to transparent (solution A). Eight replicates of solution A were prepared. The AC (6 g) was mixed with 30 mL of DMF in a 300 mL beaker and stirred at 200 rpm for 30 min to ensure even dispersion (solution B). Eight replicates of solution B were prepared. NaCl was added to each sample of solution B in increments of 0, 0.5, 1, 2, 3, 4, 5, and 6 g. Each was stirred for an additional 10 min. Solutions A and B were then combined and stirred at 200 rpm for 10 min to produce solution C, which was dried in an oven at 80 °C for 40 min, and a mixer blade measuring 75 × 17 × 1 mm was placed in the solution. With the blade immersed, 100 mL of DI water was injected evenly at six points into solution C using a syringe to solidify the polymer, as shown in Fig. 1(a). After solidification, the catalyst foam that had adhered to the blade was immersed in DI water to remove any residual DMF. The PVDF/AC-NaCl catalyst foam was initially molded into a cylindrical shape conforming to the inner shape of the beaker, as shown in Fig. 1(b). It was then cut into different shapes using a stainless-steel scalpel. For the triangular prisms, each side of the equilateral triangle was 75 mm, and the thickness was 20 mm, as shown in Fig. 2(a). The black color of the catalyst foam was due to the AC powder.

2.3 Analytical methods

Field-emission scanning electron microscopy (FE-SEM, SU5000, HITACHI, Japan) was used to analyze the surface and chemical composition of the piezocatalysts. The PVDF-based piezocatalysts were cut into pieces measuring 5 mm × 5 mm × 2 mm and placed on an FE-SEM grid with a carbon frame. Brunauer–Emmett–Teller analysis (Tristar ll 3020, Micromeritics, USA) was performed on the catalysts. The crystallinity and phase of the PVDF/AC and PVDF/AC-NaCl (NaCl: 1 g and 6 g) were defined with an X-ray diffractometer (XRD, Bruker-D8 ADVANCE) using Cu Kα radiation at 40 W and 40 kV, collecting data from 10° to 60° at a 2θ step of 0.02° and 1 s per point. X-ray photoelectron spectroscopy (XPS, PHI 5000 VersaProbe, Ulvac-PHI) was used to identify the elemental concentrations

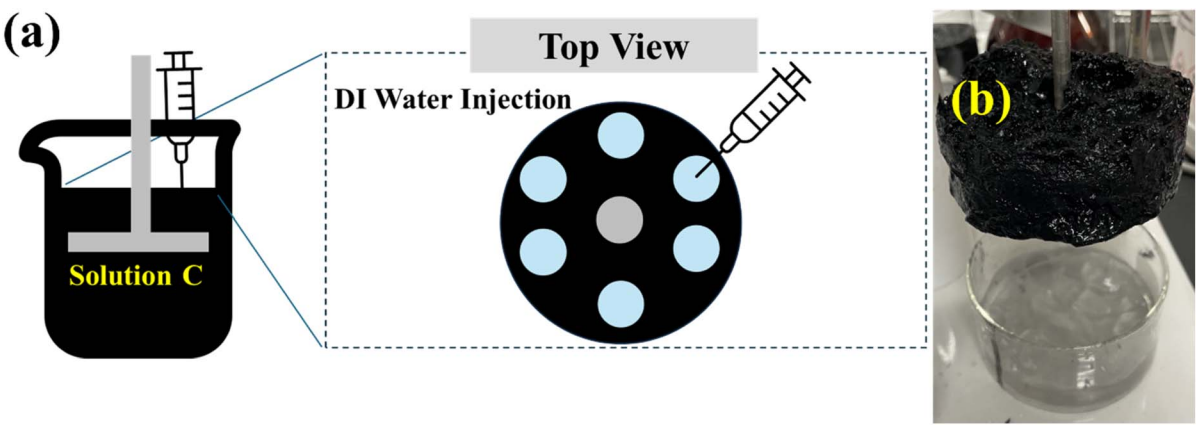

Fig. 1 (a) Schematic of deionized water being injected into a solution of PVDF/AC-NaCl dissolved in DMF and (b) the PVDF/AC-NaCl catalyst solidified in a beaker.

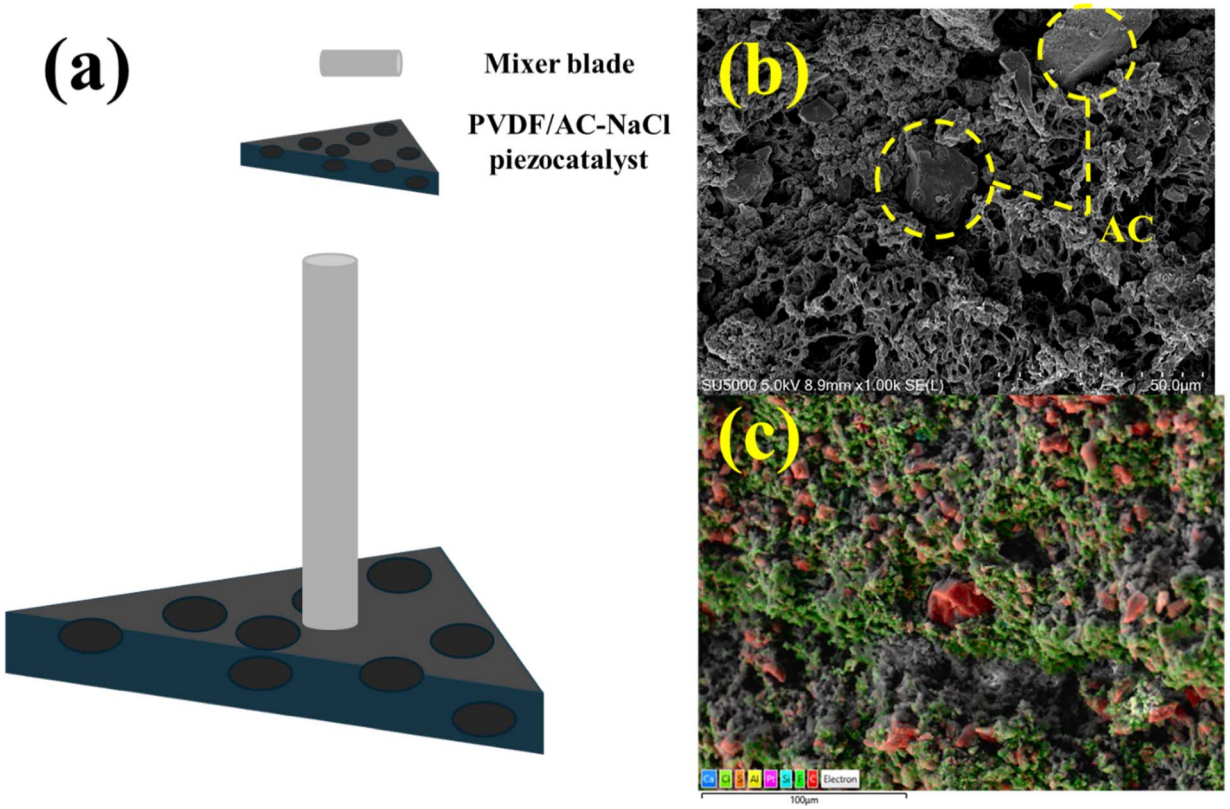

Fig. 2 (a) A schematic of the PVDF/AC-NaCl used in the experiment attached to the mixer blade, (b) an SEM image of the PVDF/AC-NaCl catalyst, and (c) an SEM-EDS image with EDS overlay, where C is depicted in red, F in green, Cl in lime green, and Pt in pink.

and functional groups of the PVDF/AC-NaCl (NaCl: 1 g) using Al Kα at 25 W and 15 kV. The photoelectron take-off angle was set at 45°. The beam sizes were 117.4 eV and 58.7 eV in survey and narrow modes, respectively. Fourier-transform infrared (FT-IR) analysis was conducted in attenuated total internal reflection mode using a diamond crystal with a resolution of 4 cm^{-1}, and 32 scans were performed to measure the phase change in pure PVDF, PVDF/AC, PVDF/NaCl (NaCl: 1 g), PVDF/AC-NaCl (NaCl: 1 g), PVDF/AC-NaCl after the cycle test, and resynthesized PVDF/AC-NaCl (LUMOS, Bruker). The piezoelectric strain coefficient (d_{33}) of the materials was analyzed using a quasi-static d_{33} instrument (YE2730A, Sinocera, China).

2.4 Piezocatalytic degradation

Piezocatalytic degradation experiments were initiated by immersing the catalyst foam-coated blade of the mixer in a 400 mL glass beaker containing 300 mL of the aqueous solution for 1 h without rotation or stirring to achieve adsorption equilibrium. The concentration of the solution with dissolved contaminants was 100 mg L^{-1}. The solution was stirred at 200 rpm with either a magnetic stirrer (iStir MS10a, 15 W, Accumax Lab Devices, India) using a 25 mm magnetic bar or with a piezoelectric catalyst attached to the mixer blade. The blade was powered by a mixer (SF 4, 60 W, M TOPS, Korea). A 3 mL aqueous sample was collected every 10 min and placed into a quartz cuvette. The samples were analyzed using a UV-visible light spectrophotometer (Evolution 350, Thermo Scientific, USA). The wavelengths were 464 nm for MO, 567 nm for RhB, 276 and 357 nm for TC, and 320 nm for 4-NIP. Phenol concentrations were detected using a gas chromatograph with a flame ionization detector (GC-FID, ChroZen GC System, Young In Chromass). The column was an HP-5 measuring 30 m × 0.32 mm × 0.25 μm (Agilent, USA). The oven temperature was maintained at 80 °C in isothermal mode, and N_2 was used as a carrier gas at a flow rate of 1.5 mL min^{-1} at 100 °C. Air and hydrogen were injected into the GC-FID at 250 °C at 300 and 30 mL min^{-1}, respectively. Liquid chromatography-mass spectrometry (6545XT advancedbio, Agilent, USA) analysis of organic contaminant degradation used a C18 column (150 mm × 4.6 mm, 5 μm, Agilent, USA). TC was analyzed using a reverse-phase setup with 0.1% ammonium formate in water (A) and acetonitrile (B), a gradient elution from 5% to 50% (B) over 20 min, a flow rate of 0.3 mL min^{-1}, and a column temperature of 40 °C. The retention time was standardized to 6 min, with detection performed in positive-ion mode using electrospray ionization. RhB, 4-NIP, and phenol were analyzed using a standard C18 configuration with 0.1% formic acid in water (A) and acetonitrile (B). Gradient elution was from 10% to 90% (B) over 15 min, with a flow rate of 0.3 mL min^{-1} and a column temperature of 35 °C. Electrospray ionization was used in positive-ion mode for RhB and negative-ion mode for 4-NIP and phenol. The electrical energy per order (E_{EO}) for contaminant degradation was calculated to determine the energy required to reduce the contaminant concentration by one order of magnitude:[41]

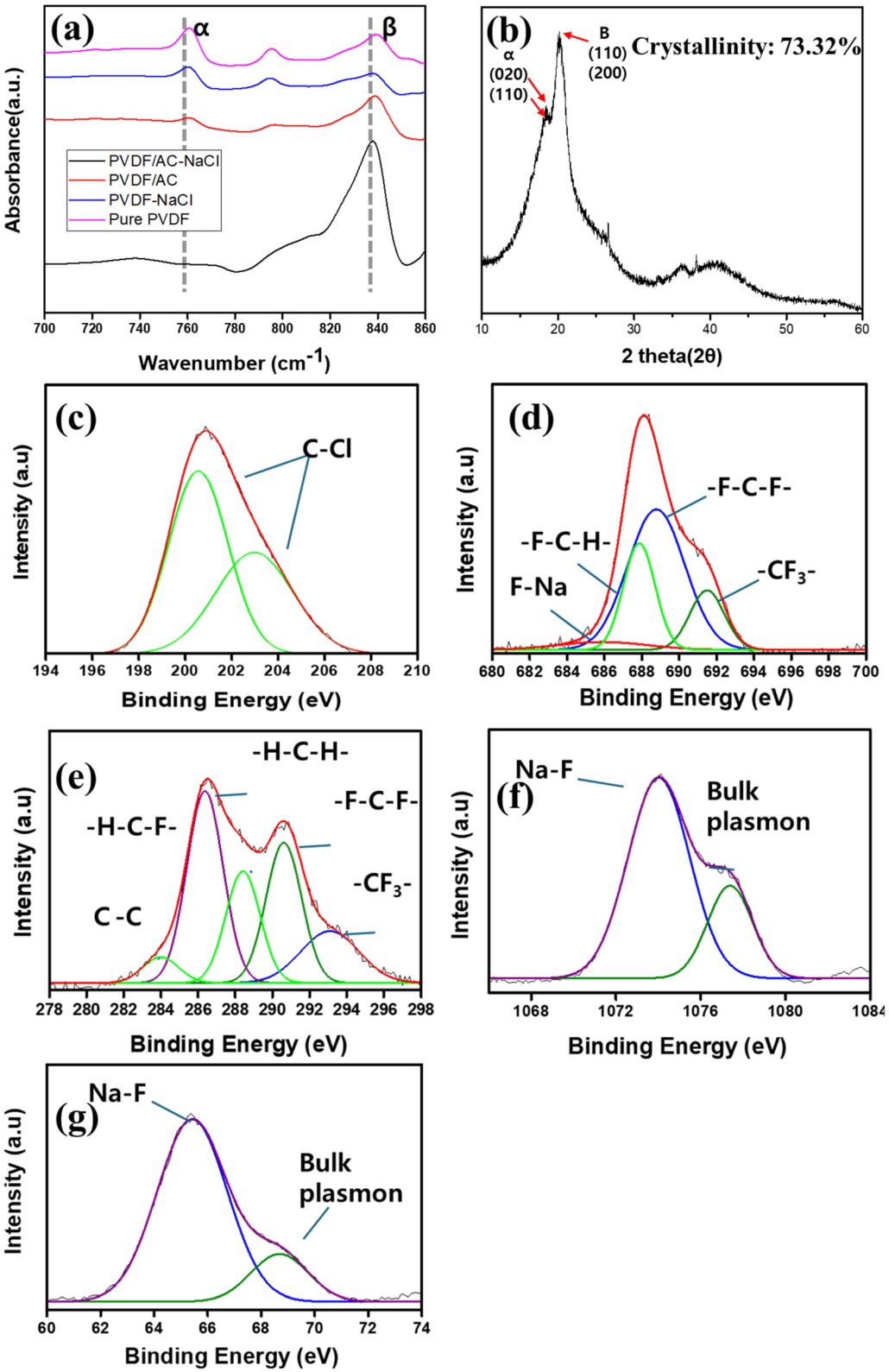

Fig. 3 (a) FT-IR spectra of PVDF/AC-NaCl, PVDF/AC, PVDF-NaCl, and pure PVDF, (b) XRD graph of PVDF/AC-NaCl. XPS spectra of PVDF/AC-NaCl, (c) Cl 2p, (d) F 1s, (e) C 1s, (f) Na 1s, and (g) Na 2s.

$$E_{EO}\ (\text{kW h per m}^3\text{ per order}) = \frac{1000W}{60V\log\left(\frac{C_0}{C_t}\right)} = \frac{1000pt}{(60V)(0.43k_1t)} = \frac{1000p}{25.80\ Vk_1} = \frac{38.76p}{k_1V} \quad (1)$$

where W is the energy consumption (J); C_0 and C_t are the concentrations at the initial and the reaction times, t (min), respectively; V is the volume of reaction solution (L); p is the input power (kW); k_1 is the pseudo-first-order rate constant (min^{-1}); and per order is the reduction in contaminant concentration on a logarithmic scale.[42]

2.5 Active species trapping

Radical quenching studies were performed to determine the key active agents in the piezocatalytic reaction. Scavengers of 10 mM thiourea, EDTA-2Na, and BQ were used to degrade MO (30 mg L^{-1}). The experiments were carried out for 30 min at 200 rpm, 15 °C, and a pH of 6.2, using either a mixer or a magnetic stirrer. Electron spin resonance (ESR, EMXplus-9.5/12/P/L System, Bruker) was conducted to monitor free radicals using DMPO and TEMPO as scavengers.

3. Results and discussion

3.1 Characterization

Fig. 2(b) is an SEM image of the PVDF/AC-NaCl used in this research. The AC particles were less than 75 μm in diameter. The presence of AC is apparent in the SEM image, along with many pores. These pores formed as the polymer was semi-crystallized due to injected DI water. The introduction of water led to a phase inversion. Fig. 2(c) is an SEM-EDS image of the catalyst. AC particles (indicated in red) are embedded on the surface. Fluorine from the PVDF on the surface is visible in green.

Fig. 3(a) depicts the FT-IR spectra of pure PVDF, PVDF-NaCl, PVDF/AC, and PVDF/AC-NaCl (1 g NaCl). The peak at 840 cm^{-1} corresponds to the β phase, while the peak at 763 cm^{-1} is indicative of the α phase. The NaCl presence in PVDF/AC-NaCl enhanced the β-phase peak intensity compared with that of PVDF/AC. The β-phase proportion needs to be high to achieve efficient PVDF piezocatalysis. The β-phase proportion ($F(\beta)$) was calculated as[43]

$$F(\beta) = \frac{A_\beta}{\left[\left(\frac{K_\beta}{K_\alpha}\right)A_\alpha + A_\beta\right]} \quad (2)$$

where A_α and A_β are the absorption values of the α phase and β phase at 763 cm^{-1} and 840 cm^{-1}, respectively. K_α and K_β are the specific absorption rates for these phases. K_α is 6.1×10^4 and K_β is 7.7×10^4 cm^2 mol^{-1}. In this research, the $F(\beta)$ was 0.544 in pure PVDF, 0.555 in PVDF-NaCl, 0.630 in PVDF/AC, and 0.755 in PVDF/AC-NaCl. This increase in $F(\beta)$ can be attributed to the polarity of DMF. Interactions between Na^+ and the carbonyl oxygen in DMF induced end charges. Similarly, the $-CF_2-$ in PVDF also carried a negative charge and was attracted to the positive charge on the fluorine atoms induced by NaCl. This attraction toward Na^+ ions encouraged the transition of PVDF to the β phase.[44] The higher $F(\beta)$ in PVDF/AC compared with pure PVDF was due to the $-CH_2-$ dipoles that were attracted to and aligned by the delocalized π electrons of AC, facilitating the transition to the β phase of PVDF. The molecular structure alignment induced by Na^+ and AC in PVDF/AC-NaCl resulted in the highest β-phase proportion.[45]

Fig. 3(b) shows the XRD pattern of PVDF/AC-NaCl (NaCl: 1 g). A combined peak was observed for the β phase (110) and (200) plane peaks at $2\theta = 20.6°$. Peaks of the α phase (020) and (110) were observed at 18.4° and 19.9°, respectively. The crystallinity of the PVDF/AC-NaCl was 73.32%.[46] The crystallinity values of pure PVDF and PVDF-NaCl were 40.74% and 52.38%, respectively (Fig. S1†). The presence of Na^+ ions and the π electrons of AC promoted alignment into the β phase and acted as nucleating agents for improved crystallinity.[44,45]

Fig. 3(c)–(g) shows the XPS spectra of the PVDF/AC-NaCl. Fig. 3(c) is the Cl 2p spectrum, in which Cl ($2p_{3/2}$) and Cl ($2p_{1/2}$) peaks are visible at 200.6 eV and 202.2 eV, respectively.[47] The chlorine from NaCl was bonded to the AC, indicating not only that the C–H bonds of PVDF were aligned by the π electrons of the AC, but also that the negative dipole moment of the C–Cl bond contributed to the alignment of the C–H bonds. Peaks indicative of –F–C–H–, –F–C–F–, and $-CF_3-$ are evident at 687.6 eV, 688.5 eV, and 691.7 eV, respectively, in Fig. 3(d). These correlate closely with the C 1s spectrum in Fig. 3(e), in which the corresponding peaks are at 288.7 eV, 292.9 eV, and 290.9 eV, respectively.[48] The –H–C–F– peak at 288.7 eV in the C 1s spectrum was the peak for unaligned monomers, and the –H–C–H– peak was at 286.4 eV.[49] The C–C peak at 283.8 eV corresponds to the bonds between carbon atoms in PVDF. The F–Na peak was observed at 685.2 eV, which corresponded to peaks at 1074.5 eV and 65.8 eV in the Na 1s and Na 2s spectra, respectively, in Fig. 3(f) and (g).[50] Additional peaks were detected at 1077.8 eV and 68.8 eV in the Na 1s and Na 2s spectra, respectively, indicating bulk plasmon.[51]

3.2 Piezoelectric properties

The measured d_{33} values of pure PVDF, PVDF-NaCl, PVDF/AC, and PVDF/AC-NaCl were 13, 16, 26, and 35 pC N^{-1}, respectively. The d_{33} was higher at a higher $F(\beta)$, confirming that a higher β-phase content led to stronger piezoelectric properties. The d_{33} of PVDF/AC-NaCl was the highest and was also higher than those of the other PVDF-based piezocatalysts synthesized by phase inversion, as shown in Table 1.[5,13,14,27,52]

Table 1 Comparison of the d_{33} of the different PVDF-based piezocatalysts synthesized using the phase inversion method

Material	d_{33} (pC N^{-1})	Reference
Fe_3O_4@MoS_2/PVDF	1.54	5
Cu_2O@MoS_2/PVDF	1.73	13
$MoSe_2$/PVDF	2.1	27
C_3N_5/PVDF	7.3	50
ZnO/CQDs/PVDF	63.2	14
PVDF/AC-NaCl	35	This study

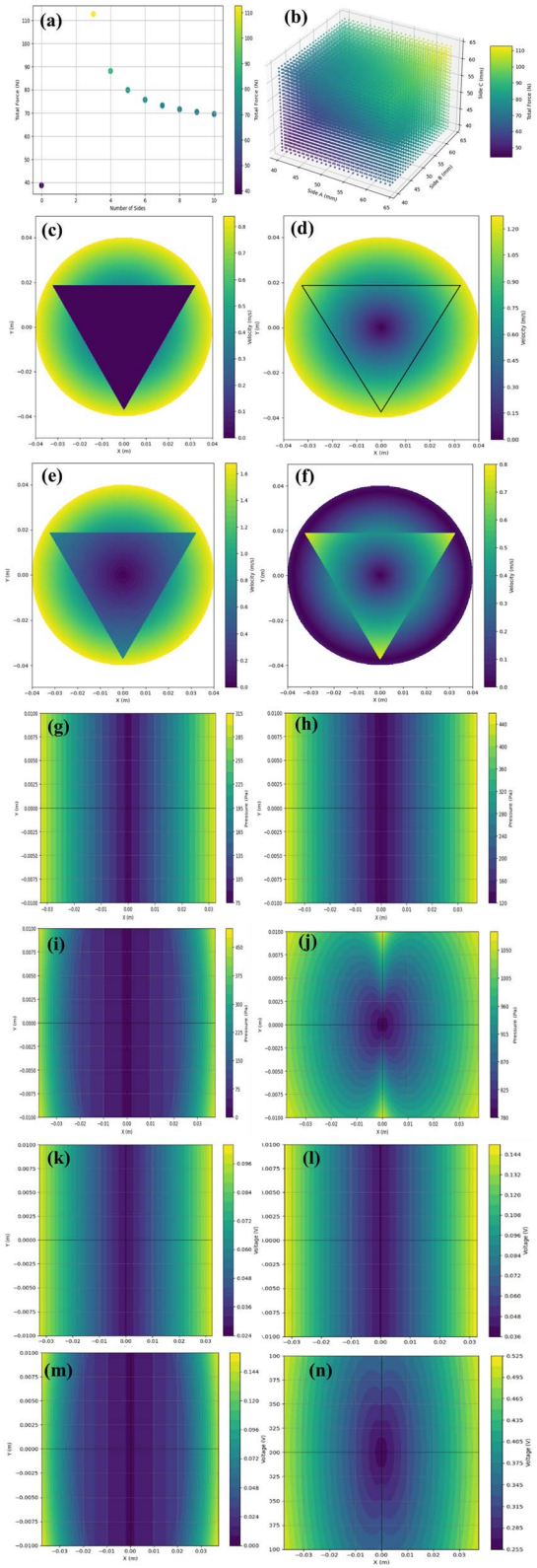

Fig. 4 (a) Calculated total force on the lateral surface of a prism *vs.* the number of sides (n) of the identical top and bottom polygonal faces. The case with 0 sides represents a cylinder. (b) Total force on the lateral surfaces of a triangular prism with identical triangular top and bottom faces. (c)–(f) The top view of the velocity distribution within a beaker in four cases. (g)–(j) Pressure distribution on one lateral surface of the PVDF/AC-NaCl triangular prism foam in the four cases. (k)–(n) Voltage generated from the PVDF/AC-NaCl triangular prism piezocatalyst lateral surface in the four cases.

The reported d_{33} of ZnO/CQD/PVDF was higher than that of the PVDF/AC-NaCl used in this research. This may be because both ZnO and PVDF are excellent piezoelectric materials, and CQDs possess excellent conductivity, although CQDs are not inexpensive.

The measured d_{33} was used to simulate the generated voltage. The total force on the lateral surfaces of n-sided equilateral prisms with identical equilateral polygonal top and bottom faces was calculated, as shown in Fig. 4(a), to identify the optimal polygonal shape for the catalyst. The circumscribed circle diameter of the n-sided polygonal was 75 mm, with a fixed height of 20 mm to fit the beaker depicted in Fig. 1(a). The total force was calculated by integrating the pressure distributed over the lateral surface areas. The total calculated force on the lateral surfaces decreased as the number of sides increased. The total force on the lateral surfaces of the triangular prism ($n = 3$) was the highest, at 112.8 N. Sharper edges and vertices of a triangular prism created significant fluid disruption, resulting in highly localized and concentrated pressure.[53] Varying lengths of the three sides of the triangle were simulated to confirm that an equilateral triangular shape was optimal, as can be seen in Fig. 4(b). The minimal length of each side was 40 mm and the maximal length was 64.95 mm, which was the length of the sides of an equilateral triangle with a circumscribed circle diameter of 75 mm. The highest total force was observed in an equilateral triangle with side lengths of 64.95 mm, which confirmed that the equilateral triangular shape was optimal.

Four configurations of equilateral triangular prism catalysts and water flow were tested in this research: (i) stationary catalyst in water rotated at 200 rpm by a magnetic stirrer, (ii) only catalyst rotated at 200 rpm in stationary water, (iii) both catalyst and water rotated at 200 rpm in the same direction, and (iv) catalyst and water rotated at 200 rpm in opposite directions. The maximal velocities in these configurations were 0.8, 1.2, 1.6, and 0.4 m s^{-1}, respectively. The velocity was lower toward the center of the beaker in cases (i–iii). In case (iv), the highest velocity was observed at the center of the side face of the catalyst, where the flow induced by the catalyst was weaker.

Fig. 4(g)–(j) depicts the pressure distribution on one side surface of the prism in four cases. The lowest pressure exerted on the side face of the triangular prism was observed in case (i). The pressure reached its highest value of 1084 Pa in case (iv). Rotating the triangular prism in the direction opposite that of the flow induced by the magnetic stirrer resulted in higher relative velocity compared to the other cases. The calculated pressure distribution was used to determine the voltage generated on the lateral surfaces of the triangular prism-shaped PVDF/AC-NaCl piezocatalyst. The voltage generated by the pressure on one lateral surface of the triangular prism is shown in Fig. 4(k)–(n). The voltage generated on each lateral face of the triangular prism was proportional to the pressure and was determined by multiplying by the g_{33} constant of 2.65×10^{-5} V m N^{-1} calculated from the d_{33}. Among the four cases, the

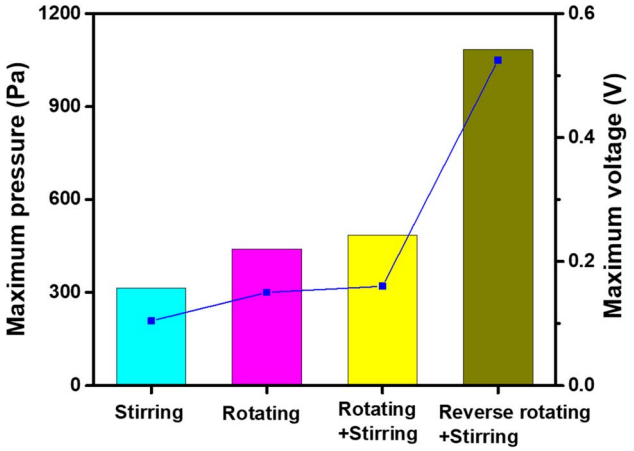

Fig. 5 Maximum pressure and maximum voltage generated in four configurations of equilateral triangular prism catalysts and water movement.

highest voltage of 0.525 V was generated in case (iv). This was approximately 2.7 times that generated by the pure PVDF catalyst, approximately 2.13 times higher than that of the PVDF-NaCl catalyst, and 1.28 times higher than that of the PVDF/AC catalyst (Fig. S2†). The distribution of voltage generation shown in Fig. 4(n) was different from the distribution of pressure in Fig. 4(j). Opposite rotations of catalyst and water movement generated turbulence, and the minor pressure caused by this turbulence led to the generation of additional voltage on the surface (Fig. S3†).[30] Fig. 5 shows the maximal pressure and voltage generated in four configurations of equilateral triangular prism catalysts and water movement.

3.3 Piezocatalytic activity of PVDF/AC-NaCl foam catalyst

Addition of NaCl to the PVDF/AC catalyst affected the catalytic efficiency, as shown in Fig. 6(a). MO degradation of approximately 81% was achieved in 30 min without the use of NaCl. The MO degradation rate was highest with the addition of 1 g of NaCl. At 0 g of added NaCl, the catalyst exhibited a crystallinity of 40.74% with lower peaks corresponding to the β phase, as can be seen in Fig. S1(a).† At 6 g of added NaCl, the catalyst produced higher peaks for the β phase compared with the catalyst with no added NaCl, as shown in Fig. S1(b).† Greater NaCl concentrations increased the nucleation points in the PVDF phase. Na^+ ions in DMF acted as nuclei, promoting polymerization and crystalline growth. However, an excess of nucleation points caused competition among nuclei, inhibiting their growth into larger crystals and reducing overall crystallinity.[44,54] This decline in crystallinity, particularly in the β phase responsible for piezoelectricity, as depicted in Fig. S1(c) and

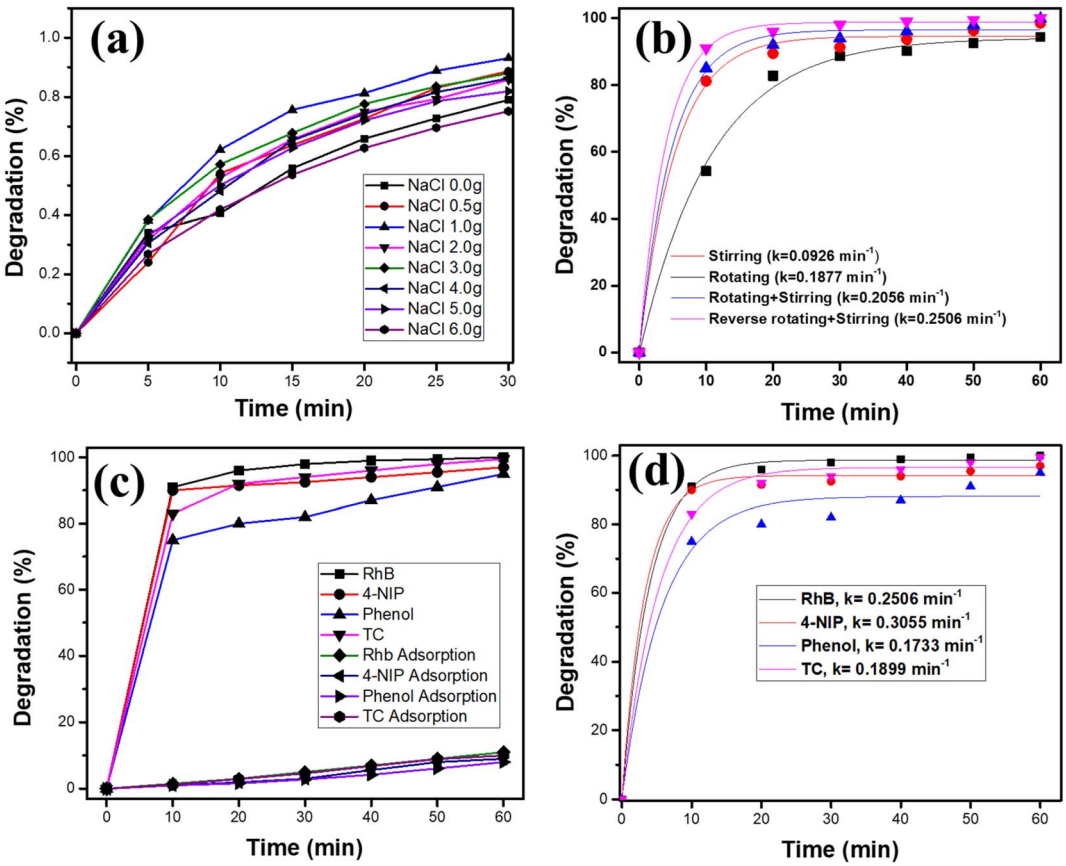

Fig. 6 (a) MO (100 mg L^{-1}) degradation kinetics at different NaCl additions, (b) RhB (100 mg L^{-1}) degradation kinetics in the four cases, (c) piezocatalytic degradation and adsorption of RhB, 4-NIP, TC, and phenol (100 mg L^{-1}), (d) pseudo-first-order kinetics in the degradation of RhB, 4-NIP, TC, and phenol.

(d),† led to decreased degradation efficiency. However, the crystallinity of 52.38% at 6 g of added NaCl was lower than that at 1 g of added NaCl, as shown in Fig. 3(b).

Degradation of RhB (100 mg L^{-1}) was compared among the four configurations, as shown in Fig. 6(b). When the first-order reaction kinetic model was fitted to the experimental results, the trend was consistent with the results shown in Fig. 4 and 5. The degradation and adsorption kinetics of RhB, 4-NIP, phenol, and TC over 60 min were monitored using the PVDF/AC-NaCl foam piezocatalyst with 1 g of added NaCl in case iv, as can be seen in Fig. 6(c). This confirmed catalytic degradation to be dominant to adsorption. The pseudo-first-order reaction-rate constants of the four contaminants were 0.2506, 0.3055, 0.1733, and 0.1899 min^{-1}, with r^2 values of 0.989, 0.981, 0.969, and 0.974, respectively, as shown in Fig. 6(d). Degradation occurred rapidly over the first 30 min.

These rate constants were used in eqn (1) to determine the E_{EO} values of RhB, 4-NIP, phenol, and TC using the catalyst developed in this research. E_{EO} is important to consider when assessing the energy consumption involved in degrading organic contaminants with a 40 W mixer and a 15 W magnetic stirrer. The calculated E_{EO} values were 38.67, 31.72, 55.91, and 51.03 (kW h per m^3 per order), respectively. The E_{EO} of TC in this research was compared with values in other studies that reported the E_{EO} of TC with different advanced oxidation processes, as in Table 2. The d_{33} of ZnO/CQD/PVDF catalyst was higher than that of the piezocatalyst listed in Table 1, but the piezocatalyst in this research was more energy-efficient than that of the ZnO/CQD/PVDF catalyst in Table 2.[5,14,55–63] The E_{EO} value of RhB, 38.67 kW h m^{-3} $order^{-1}$, was lower than that produced when using Fenton or persulfate processes (54 kW h per m^3 per order).[64] This indicates that it is possible to overcome the limitations of the material's piezoelectric properties by optimizing the geometry of the piezocatalyst and fluid movement, and that efficient organic contaminant degradation achieves the lowest energy consumption among existing advanced oxidation processes.

3.4 Reusability

A 10-cycle piezocatalytic experiment was performed for the degradation of 100 mg L^{-1} TC to evaluate the stability and reusability of the PVDF/AC-NaCl foam piezocatalyst. The TC solution was replaced with fresh solution prior to the start of each cycle. TC degradation experienced a slight decrease, achieving 85.15% degradation efficiency after the 10th cycle, as shown in Fig. 7(a). After the 10-cycle test, the PVDF/AC-NaCl foam piezocatalyst was dissolved again in a solution of 90 mL DMF and 36 mL acetone to resynthesize the new catalyst. The resynthesized piezocatalyst was associated with a recovery in degradation rate of TC to 95.78%. The pore structures and the AC attached to the surface remained intact even after the cycle tests, as revealed by SEM images before and after the cycle test, depicted in Fig. 7(b) and (c). This indicates that the AC was not leached by physical forces and the pore structure did not collapse, which explains why the piezocatalyst maintained a high degradation rate. Fig. 7(d), an SEM image of the resynthesized piezocatalyst, confirms that the pore structure observed before reuse was retained and the AC particles were reattached to the surface. The FT-IR spectra recorded before and after the cycle test are compared in Fig. 7(e) and (f), revealing that the $F(\beta)$ value decreased from 75.53% to 61.12%. Fig. 7(g), the FT-IR spectra of the resynthesized piezocatalyst, indicates that $F(\beta)$ recovered to 70.12%. The PVDF/AC-NaCl piezocatalyst maintained a high degradation rate over five cycle tests, even after resynthesis.

3.5 Piezocatalytic degradation mechanism

Radical quenching studies were conducted to identify free radicals generated by piezocatalysis. Thiourea, BQ, and EDTA-2Na were used as scavengers for ·OH, $\cdot O_2^-$, and h^+, respectively, to determine the types of active radicals involved. The addition of 10 mM quenching agents to the MO solution during the degradation experiment resulted in a decrease in degradation efficiency, as shown in Fig. 8(a). The degradation efficiency was 97.45% without added agents, declining to 82.35%, 94.24%, and 68.64% with the addition of thiourea, BQ, and EDTA-2Na, respectively. Thiourea and EDTA-2Na exhibited inhibitory effects on MO degradation, demonstrating that h^+ and ·OH were the radicals involved. The types of radicals produced using PVDF/AC-NaCl foam were analyzed through ESR. The presence of TEMPO-h^+ and DMPO-··OH was confirmed. In Fig. 8(b), the three peaks with a 1 : 1 : 1 intensity

Table 2 Comparison of energy consumption of tetracycline degradation by different processes

Material	Driving force	k (min^{-1})	P (kW)	η (%)	$E_{E/O}$ (kW h per m^3 order)	Ref
CdS/ZnO	UV	0.024	0.35	94.4	11,258.09	53
C-ZnO/CN	UV	0.054	0.15	80.1	4313.80	54
ZnO@CN	UV	0.050	0.15	97	3846.15	55
MoS_2 NTs/$CuInS_2$ QDs	Visible light	0.012	0.3	89.0	16150.00	56
$Bi_4Ti_3O_{12}$	Ultrasonic	0.010	0.18	82	6460.00	57
$K_2Ti_6O_{13}/TiO_2$	Ultrasonic	0.024	0.16	54	5168.00	58
Cu_2O/MoS_2/rGO	Ultrasonic	0.018	0.12	66	2584.00	59
MoS_2	Ultrasonic	0.025	0.11	93	1894.93	60
MoS_2/GDY	Ball milling	0.052	0.25	92.2	935.33	61
Fe_3O_4@MoS_2/PVDF pipe	Water flow	0.020	0.025	91.5	241.04	5
ZnO/CQDs/PVDF	Ultrasonic	0.058	0.3	97.9	1162.8	14
ZnO/CQDs/PVDF pipe	Water flow	0.044	0.04	95.36	176.18	14
PVDF/AC-NaCl foam	Water flow	0.190	0.04	99.54	51.03	This study

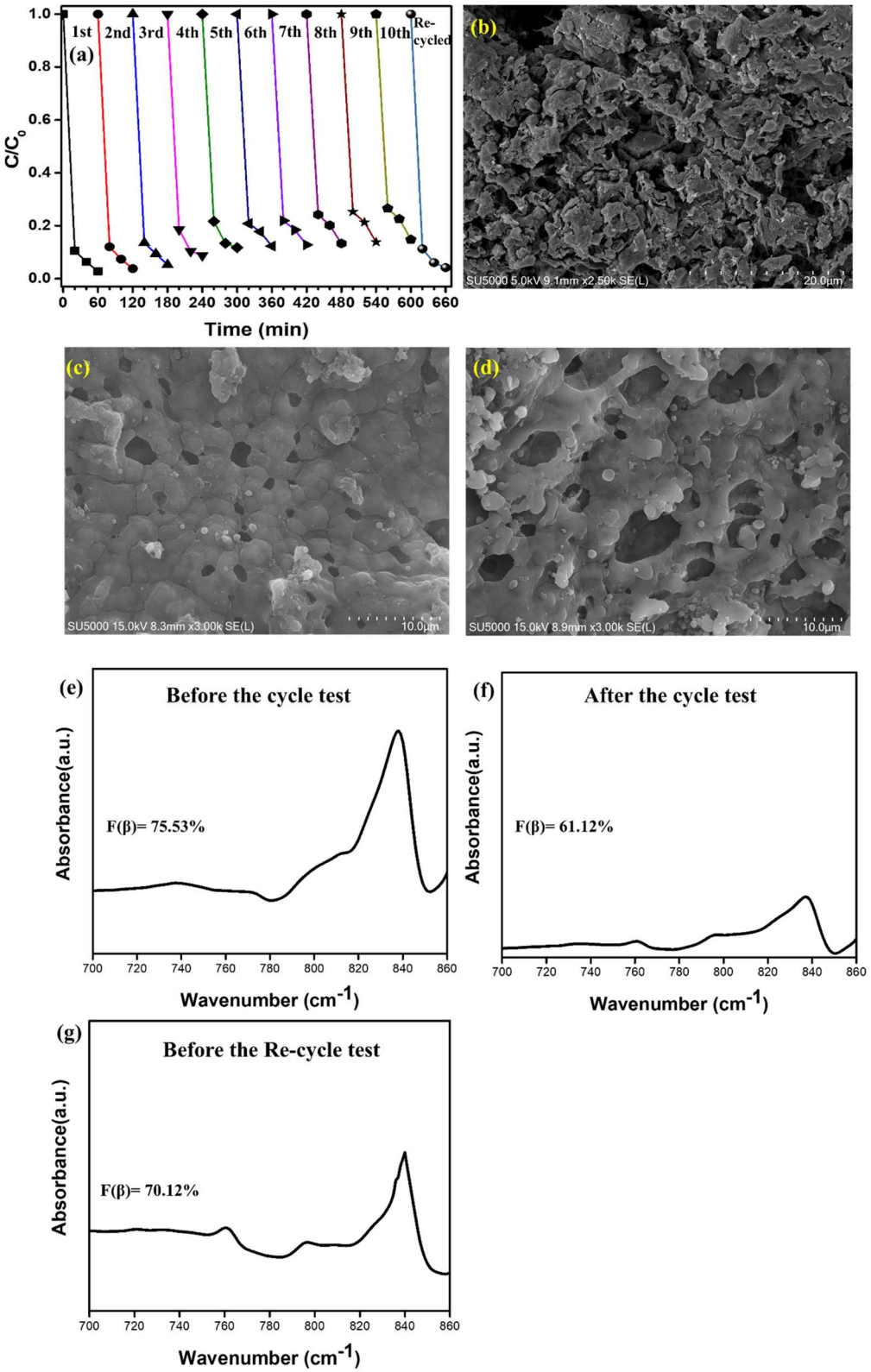

Fig. 7 (a) Reusability of the PVDF/AC-NaCl catalyst, with "re-cycle" indicating the catalyst was resynthesized after 10 repeated experiments, (b) SEM image of the PVDF/AC-NaCl catalyst before the cycle test, (c) SEM image of the PVDF/AC-NaCl catalyst after the cycle test, (d) SEM image of the re-cycled catalyst after the cycle test, (e) FT-IR spectra of the catalyst before the cycle test, (f) FT-IR spectra of the catalyst after the cycle test, (g) FT-IR spectra of the re-synthesized catalyst.

ratio can be attributed to TEMPO peaks generated by h^+.[65] In Fig. 8(c), the marked area shows a main peak with a 1 : 2 : 2 : 1 intensity ratio and three sub-peaks, indicating that ·OH radicals were generated but in smaller amounts.[66] Consequently, their intensity was approximately 10% of that seen in the TEMPO spectra, indicating lower radical production.

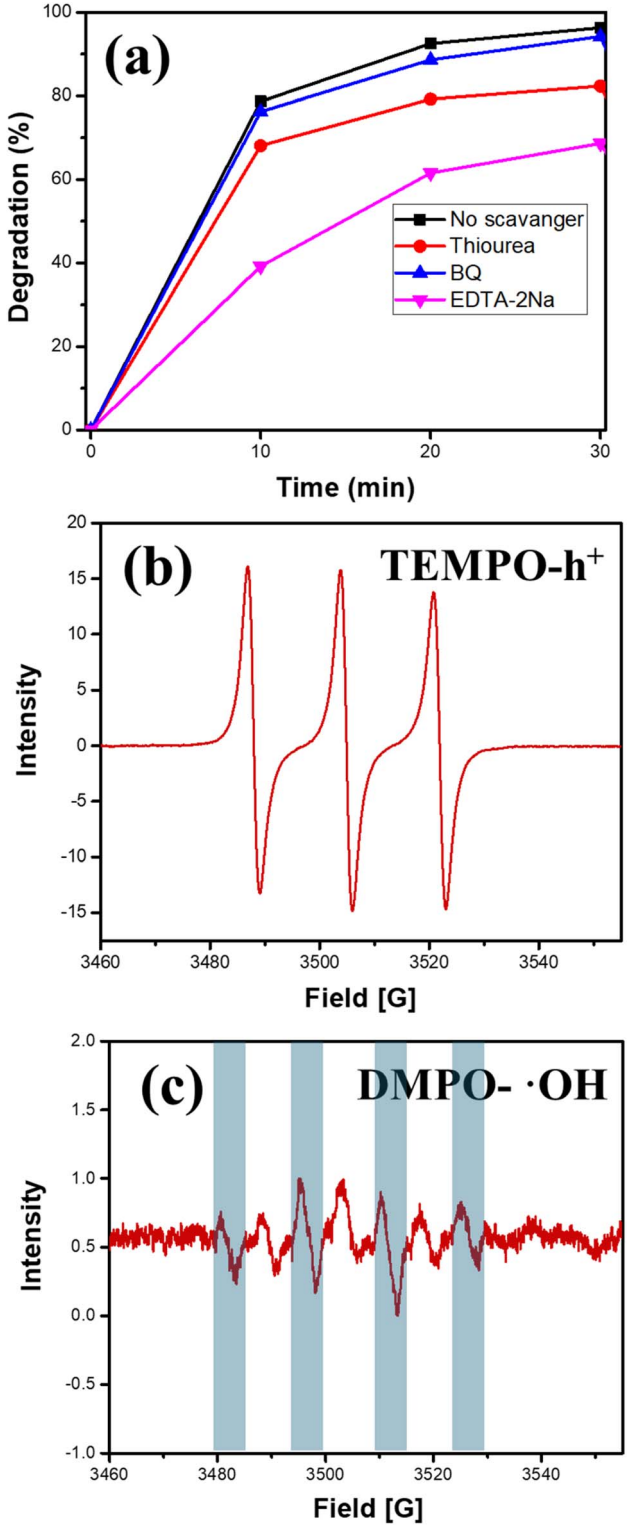

Fig. 8 (a) Active species trapping experiment. ESR spectra of radicals trapped by TEMPO and DMPO: (b) TEMPO-trapped ESR spectra of H^+ and (c) DMPO-trapped ESR spectra of hydroxyl radical (·OH).

The AC particles allowed for generation of electrons and h^+, as the β phase of PVDF was polarized under hydrodynamic external forces, leading to the creation of an internal electric field. Significant intensity difference was observed between the h^+ and ·OH radicals in Fig. 8(b) and (c), with h^+ more than 10 times more prominent. This suggested that the direct involvement of h^+ played a more direct and consequential role in initiating the degradation of organic contaminants. This may also cause the adsorption of OH^- from the solution onto the catalyst's surface, leading to the production of ·OH radicals or reaction with H_2O to generate O_2. Their absence in DMPO suggests that electrons within the catalyst bonded with Na^+ ions, while the electrons that are typically generated reacted with oxygen to form superoxide radicals.[67,68] This is proposed because the degradation rate decreased subtly in the cycle tests as in Fig. 7(a), and the β-phase ratio of PVDF was reduced as in Fig. 7(e) and (f). Binding of electrons with Na^+ ions led to a decrease in Na^+ ions that would otherwise induce the alignment of PVDF's $-CF_2-$ groups.[69] The degradation of organic contaminants in PVDF/AC-NaCl foam piezocatalysis can be expressed as

$$\text{PVDF/AC} - \text{NaCl foam} + \text{hydrodynamic force} \rightarrow h^+ + e^- \quad (3)$$

$$2H_2O + 4h^+ \rightarrow O_2 + 4H^+ \quad (4)$$

$$OH^- \text{ (fron water)} + h^+ \rightarrow \cdot OH \quad (5)$$

$$\text{Organic contaminants} + h^+ + \cdot OH \rightarrow \text{intermediates} \rightarrow CO_2 + H_2O \text{ (final product)} \quad (6)$$

The degradation of organic contaminants is illustrated in Fig. S4.†

4. Conclusion

This research emphasizes the importance of geometric optimization in enhancing the performance of piezocatalysts under fluid flow. Geometric optimization, particularly that of the triangular prism, enhanced piezoelectric response by maximizing the pressure exerted on the catalyst's surface, leading to improved catalytic activity. The catalyst's design was validated through CFD analysis and experimentally confirmed using various rotational configurations, with the reverse-direction flow achieving the highest efficiency. The triangular prism-shaped PVDF/AC-NaCl piezocatalyst, with its optimized design, exhibited a high piezoelectric strain coefficient and generated up to 5.25×10^{-1} V. The resulting h^+ and ·OH radicals contributed to the degradation of various organic contaminants, with a maximum efficiency of 99.53%. This highlights the energy efficiency of the process, with an E_{EO} of 51.03 kW h per m^3 per order. This is lower than that of conventional advanced oxidation processes, as well as piezocatalysts with higher piezoelectric strain coefficients, indicating that the system's efficiency can be enhanced through geometric

optimization rather than relying solely on material properties, resulting in high efficiency and lower energy use. The catalyst showed strong stability and reusability, maintaining 88.23% degradation after five cycles and 95.78% upon resynthesis, confirming the material's long-term operational stability. These findings provide valuable insights for piezocatalytic processes that enhance the efficiency of water treatment with minimal energy through fluid flow-induced piezoelectric effects.

Data availability

The data that support the findings of this study are available from the corresponding author upon reasonable request.

Conflicts of interest

There are no conflicts to declare.

Acknowledgements

This work was supported by the Korea Environmental Industry and Technology Institute through an Aquatic Ecosystem Conservation Research Program, funded by the Korea Ministry of Environment (No. 2021003040004).

References

1 J. Long, T. Ren, J. Han, N. Li, D. Chen, Q. Xu, H. Li and J. Lu, *Sep. Purif. Technol.*, 2022, **290**, 120861.
2 X. Ning, A. Hao, Y. Cao, J. Hu, J. Xie and D. Jia, *J. Colloid Interface Sci.*, 2020, **577**, 290–299.
3 S. Xu, W. Qian, D. Zhang, X. Zhao, X. Zhang, C. Li, C. R. Bowen and Y. Yang, *Nano Energy*, 2020, **77**, 105305.
4 E. Im, S. Park, G. Hwang, D. C. Hyun, Y. Min and G. D. Moon, *Small*, 2024, **20**(1), 2470009.
5 J. Wang, X. Zhou, J. Hao, Z. Wang, B. Huo, J. Qi, Y. Wang and F. Meng, *Appl. Catal., B*, 2023, **331**, 122655.
6 J. Shi, S. Yang, Z. Zheng, J. Li, L. Wang, W. Zeng, L. Yang, Y. Xiong, Z. Jin and X. Tao, *J. Mater. Chem. A*, 2023, **11**, 7596–7604.
7 Y. Zheng, J. Yang, B. Gong, X. Zhang, J. Li, H. Zheng, G. Chen and C. Zhao, *Chem. Eng. J.*, 2022, **441**, 136116.
8 X. Chen, J. Wang, Z. Wang, H. Xu, C. Liu, B. Huo, F. Meng, Y. Wang and C. Sun, *J. Water Process. Eng*, 2023, **56**, 104312.
9 J. Wu, Q. Xu, E. Lin, B. Yuan, N. Qin, S. K. Thatikonda and D. Bao, *ACS Appl. Mater. Interfaces*, 2018, **10**, 17842–17849.
10 E. B. Flint and K. S. Suslick, *Science*, 1991, **253**, 1397–1399.
11 M. B. Starr, J. Shi and X. Wang, *Angew. Chem.*, 2012, **124**, 6064–6068.
12 Z. Wang, W. Tong, L. Li, Y. Li, J. Yang, M. Chai, T. Cao, X. Wang, X. Wang, X. Zhang, X. Li and Y. Zhang, *Sep. Purif. Technol.*, 2023, **306**, 122768.
13 J. Wang, Y. Liang, Z. Wang, B. Huo, C. Liu, X. Chen, H. Xu, D. Li, Z. Zhu, Y. Wang and F. Meng, *Chem. Eng. J.*, 2023, **458**, 141409.
14 Z. Wang, M. Xiang, B. Huo, J. Wang, L. Yang, W. Ma, J. Qi, Y. Wang, Z. Zhu and F. Meng, *Nano Energy*, 2023, **107**, 108162.
15 Z. Ren, F. Chen, Q. Zhao, G. Zhao, H. Li, W. Sun, H. Huang and T. Ma, *Appl. Catal., B*, 2023, **320**, 122007.
16 R. W. Whatmore, *Ferroelectrics*, 1991, **118**, 241–259.
17 J. Liu, W. Qi, M. Xu, T. Thomas, S. Liu and M. Yang, *Angew. Chem.*, 2023, **135**, e202213927.
18 S. Divya, T. H. Oh and M. Bodaghi, *Eur. Polym. J.*, 2023, **197**, 112363.
19 A. Kulišťáková, *J. Water Process. Eng.*, 2023, **53**, 103727.
20 W. Lin, X. Liu, A. Ding, H. H. Ngo, R. Zhang, J. Nan, J. Ma and G. Li, *J. Water Process. Eng.*, 2022, **45**, 102468.
21 M. Abbasipour, R. Khajavi and A. H. Akbarzadeh, *Adv. Eng. Mater.*, 2022, **24**, 2101312.
22 S. Bettini, R. Pagano, D. Valli, C. Ingrosso, M. Roeffaers, J. Hofkens, G. Giancane and L. Valli, *Surf. Interfaces*, 2023, **36**, 102581.
23 M. Safaei, H. A. Sodano, S. R. Anton, M. Habib, I. Lantgios and K. Hornbostel, *J. Phys. D Appl. Phys.*, 2022, **55**, 423002.
24 P. Dong, Z. Huang, X. Nie, X. Cheng, Z. Jin and X. Zhang, *Mater. Res. Bull.*, 2019, **111**, 102–112.
25 W. Ma, B. Yao, W. Zhang, Y. He, Y. Yu and J. Niu, *Chem. Eng. J.*, 2021, **415**, 129000.
26 M. Smith and S. Kar-Narayan, *Int. Mater. Rev.*, 2022, **67**, 65–88.
27 X. Chen, A. Li, L. Xing, J. Wang, Y. Sun, Y. Wang, G. Chen, T. Xing and L. Xu, *J. Water Process. Eng*, 2024, **59**, 105015.
28 D. Jiang, M. Xu, M. Dong, F. Guo, X. Liu, G. Chen and Z. L. Wang, *Renewable Sustainable Energy Rev.*, 2019, **115**, 109366.
29 Y. J. Lee, W. K. Chong, L. K. Putri, B. J. Ng, L. L. Tan, T. Y. Wu and S. P. Chai, *Appl. Catal., B*, 2023, **334**, 122836.
30 Y. Wen, J. Chen, X. Gao, H. Che, P. Wang, B. Liu and Y. Ao, *Nano Energy*, 2022, **101**, 107614.
31 B. Liu, X. Liu, Y. Li, M. Xiao, Z. Chen, S. Wang, H. Wang and X. Wang, *Eco-Environ. Health*, 2024, **3**, 418–424.
32 T. Jiang, Y. Wang, C. Cai, C. Nie, H. Peng and Z. Ao, *Environ. Sci. Ecotechnology*, 2025, **23**, 100495.
33 R. Wang, X. Xie, C. Xu, Y. Lin, D. You, J. Chen, Z. Li, Z. Shi, Q. Cui and M. Wang, *Chem. Eng. J.*, 2022, **439**, 135787.
34 X. Xue, W. Zang, P. Deng, Q. Wang, L. Xing, Y. Zhang and Z. L. Wang, *Nano Energy*, 2015, **13**, 414–422.
35 A. C. Gadelha, A. R. Cadore, K. Watanabeal, C. Chen, Y. Xu, H. Zhao, K. A. Cunefare, E. A. Skow, A. Erturk, J. Savor, N. Verma and M. R. Cacan, *Smart Mater. Struct.*, 2013, **22**, 025036.
36 D. Rancourt and A. Tabesh, *Proc. PowerMEMS*, 2007, **20079**, 93–96.
37 X. Li, L. Zhao, J. Yu, X. Liu, X. Zhang, H. Liu and W. Zhou, *Nano-Micro Lett.*, 2020, **12**(1), 1–29.
38 Y. Du, Z. Guan, D. Chen, J. Ye, P. Li and Y. Wen, *Energy Convers. Manage.*, 2021, **250**, 114833.
39 S. K. Ghosh, A. Biswas, S. Sen, C. Das, K. Henkel, D. Schmeisser and D. Mandal, *Nano Energy*, 2016, **30**, 621–629.

40 M. G. Buonomenna, P. Macchi, M. Davoli and E. Drioli, *Eur. Polym. J.*, 2007, **43**, 1557–1572.
41 J. R. Bolton, K. G. Bircher, W. Tumas and C. A. Tolman, *Pure Appl. Chem.*, 2001, **73**, 627–637.
42 D. B. Miklos, C. Remy, M. Jekel, K. G. Linden, J. E. Drewes and U. Hübner, *Water Res.*, 2018, **139**, 118–131.
43 R. Gregorio and M. Cestari, *J. Polym. Sci., Part B:Polym. Phys.*, 1994, **32**, 859–870.
44 A. Wang, C. Chen, J. Qian, F. Yang, L. Wang and M. Zhang, *J. Electron. Mater.*, 2021, **50**, 4781–4786.
45 N. R. Alluri, A. Chandrasekhar, J. H. Jeong and S. J. Kim, *J. Mater. Chem. C*, 2017, **5**, 4833–4844.
46 C. H. Du, B. K. Zhu and Y. Y. Xu, *J. Appl. Polym. Sci.*, 2007, **104**, 2254–2259.
47 M. Wilson, R. Kore, A. W. Ritchie, R. C. Fraser, S. K. Beaumont, R. Srivastava and J. P. S. Badyal, *Colloids Surf., A*, 2018, **545**, 78–85.
48 P. Viswanath and M. Yoshimura, *SN Appl. Sci.*, 2019, **1**, 1519.
49 K. Fujitani, K. Takenaka, K. Takahara, H. Sumida, A. Yamaguchi, Y. Utsumi and S. Suzuki, *Heliyon*, 2023, **9**(5), e15794.
50 M. L. Kalapsazova, E. N. Zhecheva, G. T. Tyuliev, D. D. Nihtianova, L. Mihaylov and R. K. Stoyanova, *J. Phys. Chem. C*, 2017, **121**, 5931–5940.
51 E. Quérel, N. J. Williams, I. D. Seymour, S. J. Skinner and A. Aguadero, *Chem. Mater.*, 2023, **35**, 853–862.
52 L. Zhao, L. Li, C. Liu, W. Zhao, F. Meng, Y. Wang and Z. Zhu, *Chem. Eng. Sci.*, 2024, **287**, 119696.
53 H. Zhu, Q. Chen, M. M. Alam, T. Tang, J. Zhong and T. Zhou, *Phys. Fluids*, 2023, **35**, 57101.
54 H. H. Singh, S. Singh and N. Khare, *Compos. Sci. Technol.*, 2017, **149**, 127–133.
55 K. Jia, G. Liu, D. N. Lang, S. F. Chen, C. Yang, R. L. Wu, W. Wang and J. D. Wang, *New J. Chem.*, 2022, **46**, 11303–11314.
56 X. Huang, X. Zhang, K. Zhang, X. Xue, J. Xiong, Y. Huang, D. Zhang, J. Zhang, Z. Zhang and F. Yan, *J. Alloys Compd.*, 2021, **877**, 160321.
57 H. U. Rasheed, X. Lv, W. Wei, W. Yaseen, N. Ullah, J. Xie and W. Zhu, *J. Environ. Chem. Eng.*, 2019, **7**, 103152.
58 E. Ma, G. Sun, F. Duan, H. Wang and H. Wang, *Appl. Mater. Today*, 2022, **28**, 101504.
59 T. Cheng, W. Gao, H. Gao, S. Wang, Z. Yi, X. Wang and H. Yang, *Mater. Res. Bull.*, 2021, **141**, 111350.
60 S. Zhang, H. Liu, F. Gao, M. Fang, Y. Zhang, Y. Cai, K. Li, M. Kong and X. Tan, *J. Alloys Compd.*, 2022, **900**, 163492.
61 P. S. Selvamani, J. J. Vijaya, L. J. Kennedy, A. Mustafa, M. Bououdina, P. J. Sophia and R. J. Ramalingam, *Ceram. Int.*, 2021, **47**, 4226–4237.
62 S. Li, Z. Zhao, D. Yu, J. Z. Zhao, Y. Su, Y. Liu, Y. Lin, W. Liu, H. Xu and Z. Zhang, *Nano Energy*, 2019, **66**, 104083.
63 B. Huo, F. Meng, J. Yang, Y. Wang, J. Qi, W. Ma, Z. Wang, J. Wang and Z. Wang, *Chem. Eng. J.*, 2022, **436**, 135173.
64 W. Zhuang, Y. Zhang, Q. Luo, S. Du, B. Wu and M. Sui, *Chem. Eng. J.*, 2024, **499**, 155956.
65 J. Lu, J. Bie, S. Fu, J. Wu, Q. Huang, P. He, Z. Yang, X. Zhang, H. Zhu and P. Deng, *RSC Adv.*, 2022, **12**, 20628–20639.
66 B. Kalyanaraman, E. A. Konorev, J. Joseph and J. E. Baker, *New Compr. Biochem.*, 1994, **28**, 333–359.
67 X. Liu, L. Shen, W. Xu, W. Kang, D. Yang, J. Li, S. Ge and H. Liu, *Nano Energy*, 2021, **88**, 106290.
68 I. Janik and G. N. R. Tripathi, *J. Chem. Phys.*, 2013, **139**, 14302.
69 C. L. Liang, Z. H. Mai, Q. Xie, R. Y. Bao, W. Yang, B. H. Xie and M. B. Yang, *J. Phys. Chem. B*, 2014, **118**, 9104–9111.